The effect of Cs/FA ratio on the long-term stability of mixed cation perovskite solar cells

Dong-Hyeok Choi, Hae-Jun Seok, Su-Kyung Kim, Do-Hyung Kim, Bo Hou, and Han-Ki Kim**

D. -H. Choi, H.-J. Seok, S.-K. Kim, and Prof. H.-K. Kim
School of Advanced Materials Science and Engineering, Sungkyunkwan University (SKKU), 2066, Seobu-ro, Jangan-gu, Suwon-si, Gyeonggi-do, Republic of Korea
E-mail: hankikim@skku.edu (H.-K. Kim)

D.-H. Kim
New & Renewable Energy Laboratory, Korea Electric Power Research Institute, 34056, Daejeon, Republic of Korea
E-mail: dhkim05@kepco.co.kr

Bo Hou
School of Physics and Astronomy, Queen's Building, The Parade, Cardiff University, Cardiff, CF24 3AA, Wales, United Kingdom

Keywords: Perovskite solar cells (PSCs), Cesium, Formamidinium, mixed cation, long-term, stability

Formamidinium lead iodide ($FAPbI_3$) is ideal for highly efficient and operationally stable perovskite solar cells (PSC). However, a primary challenge for $FAPbI_3$ PSC is to suppress the phase transition from the photoactive black phase into the yellow non-perovskite δ-phase. This study demonstrates the preparation of Cs-containing mixed $FAPbI_3$ perovskite by cation stoichiometric engineering, and discusses the influence of the Cs/FA ratio on its phase stability and device performance. By exploring the optimal ratio of Cs and FA cations in $Cs_xFA_{1-x}Pb(I_{0.94}Br_{0.06})_3$ perovskite, an inverted planar device with $Cs_{0.17}FA_{0.83}Pb(I_{0.94}Br_{0.06})_3$ composition shows the best PCE of 16.5% in an active area of 1.08 cm^2. More importantly, $Cs_{0.17}FA_{0.83}Pb(I_{0.94}Br_{0.06})_3$ perovskite photoactive layer showed remarkable long-term stability, maintaining 88.1% of initial efficiency for 1,128 hours in the presence of moisture and oxygen, and without any encapsulation. The excellent long-term stability is found to originate from the appropriate tolerance factor and low thermodynamic decomposition energy, which underpins the strong potential for the commercialization of Cs-containing mixed FAPbI3

PSCs.

1. Introduction

Organic-inorganic halide perovskites, by virtue of their excellent optoelectronic properties, adjustable bandgap, long carrier lifetime, and high electron/hole mobility, have attracted significant attention in the field of solar cells [1–5]. Furthermore, because of its high power conversion efficiency and process cost reduction through solution processing, the solar cell using perovskite as a photoactive material is considered as a candidate for the next generation PV [6–12]. The best perovskite solar cell to date has achieved a high efficiency of 25.6%, which is comparable to other major thin film and silicon solar cells [13–19]. In addition, according to various cell designs, high-efficiency PSCs have been reported, and there is great potential for further efficiency improvement through cell structure enhancement [20–23].

Despite these excellent performances, the poor long-term stability of the PSCs is an obstacle to the commercialization of the solar cell, given that the benchmark life of a silicon solar cell exceeds 20 years. The most recognized decomposition pathway of perovskite materials is chemical decomposition with moisture [8]. The main causes of perovskite decomposition caused by moisture are considered to be the water absorption of the organic ammonium precursor, and the solubility of the Pb salt in water [24–26]. In addition to moisture-related decomposition, thermal decomposition, phase transition, light-induced trap state formation, and vias-induced ion migration are also important factors that hinder the stability of the perovskite solar cell [27–30]. For example, due to its low crystallization energy, the most widely used perovskite material, $MAPbI_3$, has a structural phase transition above 55 °C and rapidly decomposes upon contact with moisture, heat, and air above 85 °C [28, 31]. As a substitute for $MAPbI_3$, $FAPbI_3$ has extended light-harvesting capacity with low bandgap energy, improved thermal stability, long charge diffusion distance, and relatively high photostability [32–36]. However, $FAPbI_3$ is structurally unstable at room temperature (RT), and in the presence of oxygen and moisture, changes from the photo-active ‘black’

perovskite α-phase, to the photo-inactive 'yellow' non-perovskite δ-phase [28, 33, 37]. To stabilize the black $FAPbI_3$, mixed cation and halide systems with different compositions have been suggested [7, 35, 37, 38]. For example, when a small amount of FA^+ was replaced with MA^+ in $FAPbI_3$, the perovskite phase could be stabilized, and the interaction between the polar MA^+ and the PbI_6 octahedral cage was enhanced with higher PCEs [38]. However, the mixed cations FA^+/ MA^+ perovskite still tends to decompose by heat and moisture, which may be due to the relatively volatile nature of the methylammonium [31, 35, 37]. It has been reported that the incorporation of smaller cesium (Cs) ions into FA-based perovskites can significantly improve light and moisture stability [39–41]. Saliba et al. reported that by adding Cs^+ to the MA^+/FA^+ mixed cation perovskite, the triple cation perovskite solar cell could obtain a 21% high PCE [41]. McMeekin et al. proposed a 1.74 eV bandgap mixed cation $Cs_{0.17}FA_{0.83}Pb\ (Br_{0.4}I_{0.6})_3$ perovskite, which has long carrier life, high mobility, and high efficiency (PCE=17%) [39]. Chen et al. proposed a new single crystal composition of $(FAPbI_3)_{0.9}(MAPbBr_3)_{0.05}(CsPbBr_3)_{0.05}$, which exhibits long-term ambient tolerance to light, heat, moisture, and oxygen [42]. By mixing these various cations, research has found that the crystal structure of the hybrid perovskite can be stabilized, and such an attempt can prevent halide segregation [43]. In particular, mixed cation perovskites can be crystallized at a relatively higher temperature with higher phase stability than normal ternary perovskites ($MAPbI_3$, $FAPbI_3$, etc.) [43, 44]. However, the ratios of the mixed perovskites reported so far vary, and long-term stability studies of these Cs-containing mixed perovskite solar cells are required to commercialize PSCs.

This study investigated the optimal ratio of Cs and FA cations in $Cs_xFA_{1-x}Pb(I_{0.94}Br_{0.06})_3$, named the K5 series, and compared their photo-physics characteristics and photovoltaic performance for different cation molar ratios. In addition, their long-term stability was evaluated, which provides comprehensive evidence and support for their subsequent

commercialization. In addition, structural factors, such as the tolerance factor and thermodynamic decomposition energy of the K5 series perovskite compounds have been determined via Density Function Theory (DFT) simulations, which provide further theoretical insights into the long-term stability studies of the cation-dependent PSC.

2. Results and Discussion

We investigated the mixed cation perovskite of $Cs_xFA_{1-x}Pb(I_{0.94}Br_{0.06})_3$ with different Cs:FA molar ratios including (K5A, K5B, K5C, and K5D) at Cs:FA= (10:90, 17:83, 24:76, and 31:69) %/%, respectively. **Figure 1**a shows X-ray diffraction (XRD) patterns of the K5 series perovskite materials. Typical perovskite characteristic peaks of (14.7, 20, 24, 28, and 32)° were observed in all samples. This is consistent with the typical photoactive 'black' α- phase FA-based mixed perovskite, while the photoinactive hexagonal yellow δ-phase peak of 11.6° degrees was not observed in any sample. However, in the K5A sample in which the molar ratio of Cs is 0.10, a side peak of cubic PbI_2 was observed at 12.7°. In addition, strong peaks of K5A and K5B were observed at 14.7°, which is the preferential orientation of the K5 series, and represents the (110) plane. The photoluminescence (PL) spectra in **Figure 1**b are blue-shifted by ~35 nm from K5A to K5D according to the molar ratio of Cs. To investigate the band energies of the K5 series perovskite film, ultraviolet photoelectron spectroscopy (UPS) was performed. Specifically, the work function (WF) and valence band (VB) level were obtained from their secondary electron cutoff (SEC) and the Fermi edge valence band maximum (VBM) spectra (shown in **Figure S1** of the Supporting Information (SI)), on account of the expressions $WF = 21.2\ eV - E_{cutoff}$ and $VB = 21.22\ eV - (E_{cutoff} - E_{edge})$ [45]. **Figure 1**c shows a schematic of the energy band diagram of the K5 series based on the UPS examination results. By increasing the Cs molar ratio, the band energies from K5A to K5D are changed from (1.57, 1.60, and 1.62, to 1.64) eV, which is consistent with the tendency of the PL results. **Table 1** summarizes the Cs/FA ratios and band energies of the K5 series

perovskite compounds. Figure 1 shows that the Cs cation was successfully integrated into the FA-based perovskite lattice. Since the ionic radius of inorganic Cs is 1.81 Å, which is smaller than the 2.79 Å of FA, the binding of Cs and FA cations reduces the ionic radius of the cation in the perovskite. It is assumed that this decrease in ionic radius leads to a change in the tolerance factor, and is induced by the stable cubic structure perovskite of the photoactive α-phase. This explanation is in good agreement with the other studies on mixed cation PSCs [8, 40, 46]. Li et al. also reported that the tolerance factor of the FA-based perovskite changes as a function of the Cs content associated with the phase transition between α and δ-phase [8].

Figure 2 shows the local atomic structure, geometric factors, and decomposition energies (ΔH_D) of the K5 series. Several factors can affect the stability of the perovskite material, and the structural stability is known to be particularly important [47–49]. In general, the perovskite structure of ABX_3 has a different crystal structure depending on the interaction between A cation and the corner-sharing BX_6 octahedra, as well as the ionic radius of A & B cations and X anions. A geometrical parameter called the tolerance factor (t) introduced by V.M. Goldschmidt in 1926 is a reliable empirical indicator that can predict the stability of crystal structures [50]. The tolerance factor can be calculated from each ionic radius using the following equation:

$$t = \frac{r_A + r_X}{\sqrt{2}\,(r_B + r_X)}$$

where, r_A and r_B are the ionic radii of the A and B cations, respectively, and r_X is the ionic radius of the anions. In general, when the tolerance factor value is in the range (0.9–1.0), it is considered as an ideal cubic structure material. The perovskite material tends to have an orthorhombic structure at $t < 0.8$, a cubic structure at $0.8 < t < 1$, and a hexagonal structure at $t > 1$. Another factor for more accurately predicting the stability of the perovskite crystal structure is whether the B site cation has a size suitable for coordination with six X site anions [51]. To evaluate the suitability of B site cations for X6 octahedrons, the following octahedral

factors have been utilized[52]:

$$\mu = \frac{r_B}{r_X}$$

In general, it has been reported that when μ > 0.41, a perovskite structure is formed [53]. Structural maps of perovskite materials can be depicted with plots of t and μ, which can be used to predict the geometric stability of perovskite. Here, although the t and μ maps represent qualitative descriptors of the perovskite stability, there are limitations in providing quantitative descriptors. Sun et al. suggested the $t+\mu$ and $(t+\mu)^{\eta}$ indices representing the thermodynamic stability of perovskite, where η is the atomic packing fraction (APF) defined by the following equation [54]:

$$\eta = \frac{V_A + V_B + 3V_X}{a^3}$$

where, V_A, V_B, and V_X are the atomic volumes of A, B, and X ions, respectively, and based on the rigid sphere model, a is the lattice constant of the cubic cell using the following equation [55]:

$$a = 2\beta(r_B + r_X) + \gamma t - \delta$$

where, the values of β, γ, and δ are the empirical coefficients given in Ref. [55]. In particular, in a rigid sphere model, higher APF values increase the probability of achieving a stable crystal structure. Therefore, it is proposed that the $(t+\mu)^{\eta}$ index can more accurately predict the stability of the crystal than can the $(t+\mu)$ index. The authors maintained that the thermodynamic stability of perovskite can be predicted with an accuracy of 86 % or more through decomposition energy (ΔH_D) based on DFT calculation and plots of $t+\mu$ and $(t+\mu)^{\eta}$. We calculated the geometric factors of the K5 series perovskite using the above equations,

and the effective radius value generally known according to the previous literature [54–56]. In addition, the decomposition energy related to the thermodynamic stability of perovskite was also calculated using the equation reported in the literature [54]. **Figure 2**b shows the tolerance factor of the K5 series perovskite calculated from the ionic radii of A, B, and X. Figures 2c & d show the results of plotting t+μ, (t+μ)η, and the decomposition energies, respectively. Figure 2b shows that when a small Cs cation with a size of 1.81 Å is inserted into the lattice of a large FA cation with 2.79 Å, the tolerance factor increases as the amount of Cs increases. All K5 series perovskite samples have a tolerance factor of > 0.9, which can be considered to present ideal crystallographic stability. **Figures 2**c & d show the results of plotting $t+\mu$, $(t+\mu)^{\eta}$, and the decomposition energies, respectively. **Figure 2**b shows that when a small Cs cation with a size of 1.81 Å is inserted into the lattice of a large FA cation with 2.79 Å, the tolerance factor increases as the amount of Cs increases. All K5 series perovskite samples have a tolerance factor of > 0.9, which can be considered to present ideal crystallographic stability. **Figures 2**c & d confirm that the perovskite material's decomposition energy and $t+\mu$, $(t+\mu)^{\eta}$ have a linear relationship, which is consistent with that reported in the previous literature [54]. The high decomposition energy of perovskite indicates good structural stability. For the K5 series compounds, as the Cs cation content decreased, the decomposition energy increased. In particular, K5A and K5B with Cs molar ratios of (0.10 and 0.17), respectively, exhibited appropriate $t+\mu$ and $(t+\mu)^{\eta}$ values, and their high decomposition energy could predict thermodynamic stability. From these results, we were able to tune the structural parameters and thermodynamic decomposition energy of perovskite by mixing Cs and FA cations in an appropriate molar ratio, and secured a stabilized α-phase FA-based mixed perovskite. This can be seen from the characteristic peak of the perovskite α-phase of the XRD results in **Figure 1**a. **Table 2** summarizes the calculated structural factors and decomposition energies of the K5 series mixed perovskite compounds.

The perovskite surface morphology was confirmed through atomic force microscopy (AFM) and scanning electron microscopy (SEM) analysis. **Figures 3**a & b show two-dimensional AFM images and root mean square roughness (RMS) values of the perovskite film. The average RMS values of K5A–K5D were (18.06, 12.98, 22.34, and 16.76) nm, respectively; among them, the RMS value of K5B was the lowest. **Figures 3**c & d show a cross-sectional SEM images of the planar structured perovskite solar cell employing K5B ($Cs_{0.17}FA_{0.83}Pb(I_{0.94}Br_{0.06})_3$) active layer, and surface SEM images of the K5 series perovskite films, respectively. **Figure 3**c shows that the PSCs with the K5 series perovskite is the film layer is formed uniformly, and the K5B perovskite layer is formed to a thickness of about 520 nm. In addition, it can be seen from **Figure 3**d that the K5 series perovskite grains with a size of > 300 nm uniformly cover the surface. Interestingly, the grain size of K5D with the highest Cs molar ratio was > 500 nm, which was the largest of the K5 series perovskite compounds. This phenomenon is presumed to be because an adequate amount of Cs ions contributes to the seed generation of perovskite crystals at RT. Saliba et al. reported that a small amount of CS in the triple cation perovskite of CS/MA/FA becomes a seed for a uniform perovskite film [37]. These results confirm that the Cs-containing mixed perovskite K5 series thin film morphology and surface morphology were excellent.

Ultraviolet–visible (UV–Vis) analysis was performed to confirm the optical properties of the K5 series mixed perovskite (**Figure S2** of the SI). The absorption spectra of K5A and K5B with Cs molar ratios of (0.10 and 0.17), respectively, in most of the visible light region, appeared strong and red-shifted at the absorption edge, as shown in **Figure S2**a of the SI. This UV–VIS spectrum is consistent with the trend of the PL results in **Figure 1**b, and is likely due to the small bandgaps of K5A and K5B. In addition, the transmittance in **Figure S2**b of the SI was observed to have a tendency opposite to that of the absorption spectra, and showed semi-transparent characteristics in the visible light region, as shown in the inserted photo.

The performance of the solar cell was evaluated by fabricating PSCs using K5 series

perovskite as a photoactive layer. PSCs were fabricated in the form of inverted planar p–i–n structures with an active area of 1.08 cm^2 and device size of 2.5 cm × 2.5 cm. The SI shows the fabrication details, structure, and photos of PSCs. **Figure S3**a of the SI shows that the K5 series perovskite (~500 nm thick) was coated on the ITO/glass deposited with a NiO hole transfer layer (HTL) (~30 nm). Fullerene C_{60} as an electron transport layer (ETL) and silver as a top metal electrode were then deposited by thermal evaporation. To prevent corrosion due to contact between the top metal electrode and the perovskite photoactive layer, a SnO_2 thin film was deposited on the ETL by a thermal evaporation process. Figures S3b & c of the SI show the solar cell structure applied with the K5 series photoactive layer and pictures of the final device, respectively.

Figure 4a compares the photovoltaic performance of PSCs using the K5 series perovskite measured under the simulated light of 1 sun (100 mA/cm^2) illumination for each parameter of the open-circuit voltage (Voc), short circuit current (Jsc), fill factor (FF), and power conversion efficiency (PCE). The Voc and Jsc results agree with the bandgap and PL data of the K5 series perovskite. In other words, as the Cs ratio decreases, the bandgap decreases, resulting in lower Voc, while the red-shifted absorption wavelength increases the Jsc. On the other hand, FF showed a slightly different trend from the other parameter values, especially K5B, which showed the highest value. This may be due to the structural stability and morphology of the perovskite layer of K5B device. As shown in **Figure 2**, the tolerance factor and decomposition energy of K5A and K5B were excellent, and the strongest α-phase perovskite peak was observed at 14.7° of K5B through the XRD result of **Figure 1**a. In the K5A sample in which the molar ratio of Cs is 0.10, a side peak of cubic PbI_2 was observed at 12.7°. From these results, it can be inferred that K5B has excellent structural and crystallographic stability and contributed to the high FF. In addition, **Figure 3**b shows that the RMS value of K5B is the lowest, which means that the perovskite film has a relatively uniform surface. Accordingly, it is estimated that the surface coverage of the electron transfer

layer above the perovskite increases, and the interfacial resistance decreases, resulting in high FF. This can also be inferred from the lowest FF of K5C, which has the highest RMS value, and the roughest film surface. As a result, the PCE of the solar cell applying the K5 series perovskite showed an efficiency of (13.5 to 16.5) %. At this time, as a result of the evaluation of PSCs to which K5B (RMS: 10.41 nm) and K5C (RMS: 9.11 nm) of film quality having similar RMS values were applied, it was confirmed that the performance of K5B was clearly excellent with PCE of 16.5% and 12.8%, respectively.

To check the reproducibility, Ten PSCs were prepared per sample, the photovoltaic parameters were measured, and an average value was obtained. In particular, PSC with K5B showed the best performance, as follows: Voc of 1.03 V, Jsc of 22.2 mA/cm^2, fill factor of 71.8%, and PCE of 16.5%. Moreover, the solar cell's performance can also be confirmed through the J–V curve in **Figure 4**b. The best performing PSC with K5B showed the reliable hysteresis with a difference of under 1% in the efficiency between the forward scan and reversed scan under standard AM1.5G conditions as shown in **Figure S4**. As described above, it is estimated that because of the relatively good structural stability and morphology of K5B, which results in an enhanced interfacial coverage for the ETL, as well as a reduction of the series resistance, the film quality of the photoactive layer is excellent. In addition, EQE measurement for the K5 series mixed perovskite compound found that it was stabilized by more than 80% in the wavelength range of about (410–800) nm (**Figure 4**c). The cut-off wavelength of each sample was around 800 nm, and the trend was consistent with the PL result (**Figure 1**b), where, as the Cs molar ratio decreased, a redshift of the wavelength was observed. **Table 3** summarizes the photovoltaic parameters derived from the J–V curve of PSCs using the K5 series perovskite active layers.

Finally, **Figure 5** shows that we investigated the long-term stability of PSCs using the K5 series with different Cs and FA ratios as photoactive layers. Long-term stability was evaluated in an air atmosphere at RT with a relative humidity of (45–55) % for the device without

encapsulation. Moreover, **Figure S5** of the SI additionally shows the long-term stability trend for each photovoltaic parameter of the PSCs to which the K5 series perovskite was applied. To confirm the reproducibility, three PSCs were prepared for each sample, and a long-term performance evaluation was performed to obtain an average value. The device performance was evaluated at intervals of about (100–300) h under light illumination (100 mW cm^{-2}). **Figures 5**a & b show the trends of PCE and normalized PCE over 1,000 h, respectively. Some of the PSCs to which the K5 series perovskite was applied showed an increasing PCE tendency compared to the initial stage, which is believed that NiO was oxidized in the air atmosphere, reducing oxygen vacancy, which resulted in reduced interfacial resistance with the perovskite photoreactive layer. Chang et al. reported that PSC with NiO as HTL increased stability in the air atmosphere [57]. In the long-term performance evaluation, the PSC applied with K5A and K5B maintained (76.4 and 88.1) %, respectively, of the initial efficiency after 1,128 hours, showing excellent durability, even without encapsulation. We suggest that this is because K5A and K5B exhibit appropriate $t+\mu$ and $(t+\mu)^{\eta}$, as shown in **Figures 2**c & d, respectively, and are structurally and thermodynamically stable with low decomposition energy. We can also confirm that the efficiency of K5C and K5D decreases with time, as predicted through structural factors, such as tolerance factors and decomposition energy. In addition, in **Figure 1**a, the XRD peak of 14.7° on the (110) plane of K5A and K5B was strong. We suggest that the preferential crystallinity of the materials is high, which influenced the structural stability of perovskite. In other words, the stable 'black' α-phase FA of the K5A and K5B mixed perovskite is thought to have contributed to the long-term stability of PSC. In particular, the long-term stability of K5B was the best, and **Figure 5**c and **Table 4** show the J–V curve and the photovoltaic parameters of PSC with K5B as a function of time, respectively. At 1,128 hours after the stability evaluation of the perovskite solar cell was completed, the relative degradation of FF in the photovoltaic parameter of K5B was the largest at 14.2%. This result is inferred, because some of the upper Ag electrodes in the p–i–n

reverse planar solar cell penetrated into the perovskite layer, and reacted with iodide to cause corrosion [58, 59]. The corrosion properties of the device induced by the Ag upper electrode can be observed in **Figure 5**d from the photo of the change in appearance over time of the PSC with the K5 series. To solve the problem of penetration and corrosion of the upper metal electrode of the perovskite in the future, we plan in future work to investigate the introduction of conductive oxides, such as ITO, as a protective layer on the top of the ETL [60]. Moreover, to secure the durability of PSC, it is necessary to apply gold as the upper electrode instead of silver, which due to its high reactivity with the iodide, causes corrosion of the device. In addition, to improve the durability of PSC with the K5 series photoactive layer, we intend to conduct solar cell stability evaluation based on tests such as the IEC61646 damp heat test, after applying encapsulation.

Figure 6 shows the appearance and cross-sectional TEM images of an inverted planar PSC of the Glass/ITO/NiO/perovskite/C_{60}/Ag structure using K5 perovskite before and after the stability evaluation test. It is evident through the clearly distinguished interface between each thin film layer in the cross-sectional TEM image that interdiffusion between the layers did not occur. In addition, we can confirm that the K5 series perovskite layer is uniformly and smoothly coated on the top of the NiO as the HTL. **Figures 6**b & c show the enlarged interface between the thin film layers indicated by the square dotted line in the PSCs before and after the stability evaluation, respectively. In region 'A' of **Figures 6**b & c, good contact is shown between the SnO_2:Ag cathode layer, the C_{60} layer as the ETL, and the K5B perovskite layer; and after stability evaluation of the PSCs, no collapse of the interface is observed. Enlarged images and fast Fourier transform (FFT) patterns of about 500 nm thickness K5B perovskite layers obtained from regions 'B', and 'C' of **Figures 6**b & c are also provided. The enlarged image and FFT pattern can confirm that even after 1,128 hours, the crystallinity of the perovskite layer is maintained. In the 'D' region, which is the lower layer of the inverted planar PSC, the K5B perovskite layer, the HTL, and the lower ITO transparent

electrode are well distinguished, so interdiffusion did not occur; and after the stability test of the PSC, no decomposition was observed.

3. Conclusion

In summary, we investigated the optimal ratio of the Cs and FA cations in the $Cs_xFA_{1-x}Pb(I_{0.94}Br_{0.06})_3$, named K5 series, a series of Cs-containing mixed perovskite compounds. In particular, the optoelectronic properties and photovoltaic performance according to different cation molar ratios were compared. As a result of evaluating the performance of the inverted planar device with $Cs_{0.17}FA_{0.83}Pb(I_{0.94}Br_{0.06})_3$, the optimal composition perovskite composition named K5B showed the best PCE of 16.5% in the photoactive area of 1.08 cm^2. More importantly, the PSC with K5B perovskite photoactive layer showed excellent long-term stability, maintaining 88.1% of initial efficiency for 1,128 hours in the presence of moisture and oxygen, without encapsulation. In future work, we intend to replace the highly corrosive upper electrode silver with gold for the p–i–n inverted planar structure PSC applied with K5 series perovskite, and sputter deposit ITO on the top of the ETL as a perovskite protective layer. In addition, to further improve the durability of the PSC with the K5 photoactive layer, we will conduct the solar cell stability evaluation based on IEC61646 after encapsulation. In conclusion, we confirm the commercialization potential of the PSCs with the excellent long-term stability of the K5 series photoactive layer. We propose that the K5B perovskite compound shows a positive effect on the long-term stability of PSCs with good structural factors, such as an appropriate tolerance factor, and low thermodynamic decomposition energy.

4. Experimental Section

Analysis of perovskite and PSCs: The crystallographic properties of the K5 series perovskite materials were analyzed by X-ray diffraction (XRD: D8 ADVANCE, Bruker) with Cu–Kα radiation. The photoluminescence (PL) spectra of the as-prepared perovskite with different Cs

and FA molar ratios were acquired by FLS980 spectrometry (Edinburgh Instruments), and the extracted optical bandgap of perovskite was compared using ultraviolet photoelectron spectroscopy (UPS: ESCALB-250Xi, Thermo). The perovskite surface morphology and cross-sectional imagery of PSCs were observed by atomic force microscopy (AFM: SPA400 SPM, Seiko Instrument) and field emission scanning electron microscopy (FESEM: JSM- 7600F, JEOL), respectively. In addition, high-resolution transmission electron microscopy (HRTEM: JEM-2100F, JEOL) analysis was performed to confirm the change in the microstructure of the perovskite and the interfacial structure between the thin film layers before and after the stability evaluation test of the PSCs. The absorption and transmission spectra of the perovskite photoactive layer film were measured by UV/visible spectrometry (UV-670, Jasco).

Fabrication of perovskite solar cells: **Figure S3** of the SI shows a schematic of the PSC fabrication process with K5 mixed perovskite compounds. A commercial substrate (AMG, Korea) on which NiO (HTL) was deposited by a sputtering process on an ITO transparent anode was heated at 300 °C for 30 min. A 1.45 M $Cs_xFA_{1-x}Pb(I_{0.94}Br_{0.06})_3$ perovskite precursor solution was prepared by mixing PbI_2, FAI, and CsBr materials in N,N- dimethylformamide (DMF) and dimethyl sulfoxide (DMSO) (8:2 v/v) solvent. The perovskite solution was coated on the prepared NiO/ITO substrate by a continuous two-step spin coating process of (500 and 5,000) rpm for (5 and 45) s, respectively. In the second spin coating step, 250 μL of anhydrous chlorobenzene was added to the substrate after 35 s, and dried at 150 °C for 10 min. Then, C_{60} as ETL and SnO_2 as a perovskite protective layer were deposited on the perovskite photoactive layer with a thickness of (35 and 4) nm, respectively, under a vacuum of 1×10^{-6} Torr using a thermal evaporation system (ITS-THS-3-50, I.T.S.). As a final step, a 120 nm thick Ag metal was also deposited on the SnO_2 layer by thermal evaporation to form an upper cathode. During PSC fabrication, a square metal shadow mask was used to pattern the 1.08 cm^2 active area.

Evaluation of perovskite solar cells: The J–V characteristics of the devices were measured by Keithley 4200 source meter under AM 1.5 G (100 mW/cm^2) light simulated by an Oriel solar simulator (Newport, class AAA solar simulator). The light intensity was calibrated using a Si solar cell certified by the National Renewable Energy Laboratory. All of the device characteristic measurements were conducted in ambient air. In addition, the external quantum efficiency (EQE) of the PSCs was measured using a QTest Station 2000ADI system (Crowntech Inc.).

Supporting Information

Supporting Information is available from the Wiley Online Library, or from the corresponding authors.

Acknowledgements

This work was supported by the Korea Electric Power Corporation (KEPCO, CX72170049). This study also received partial support from the Korea Electric Power Corporation (KEPCO, R20XO02-7). This work was also supported by a Korea Basic Science Institute (KBSI) National Research Facilities & Equipment Center (NFEC) grant, funded by the Korea government (Ministry of Education) (No. 2019R1A6C1010031).

References

[1] H. Zhang, X. Ren, X. Chen, J. Mao, J. Cheng, Y. Zhao, Y. Liu, J. Milic, W.-J. Yin, M. Grätzel, W. C. H. Choy, *Energy Environ. Sci.* **2018**, *11*, 2253.

[2] Q. Zhang, Y. Yin, *ACS Cent. Sci.* **2018**, *4*, 668.

[3] L. Liu, S. Huang, Y. Lu, P. Liu, Y. Zhao, C. Shi, S. Zhang, J. Wu, H. Zhong, M. Sui, H. Zhou, H. Jin, Y. Li, Q. Chen, *Adv. Mater.* **2018**, *30*, 1800544.

[4] A. Kojima, K. Teshima, Y. Shirai, T. Miyasaka, *J. Am. Chem. Soc.* **2009**, *131*, 6050.

[5] J.-G. Kim, J.-H. Lee, S.-I. Na, H. Lee, Y. Kim, H.-K. Kim, *Org. Electron.* **2020**, *78*, 105560.

[6] Y. Zhao, K. Zhu, *J. Phys. Chem. Lett.* **2014**, *5*, 4175.

[7] W. S. Yang, J. H. Noh, N. J. Jeon, Y. C. Kim, S. Ryu, J. Seo, S. I. Seok, *Science* **2015**, *348*, 1234.

[8] Z. Li, M. Yang, J.-S. Park, S.-H. Wei, J. J. Berry, K. Zhu, *Chem. Mater.* **2016**, *28*, 284.

[9] D.-H. Choi, H.-J. Seok, D.-H. Kim, S.-K. Kim, H.-K. Kim, *Sci. Technol. Adv. Mater.* **2020**, *21*, 435.

[10] H.-J. Seok, A. Ali, J.-H. Seo, H.-H. Lee, N.-E. Jung, Y. Yi, H.-K. Kim, *Sci. Technol. Adv. Mater.* **2019**, *20*, 389.

[11] H.-J. Seok, H.-K. Kim, *Metals* **2019**, *9*, 120.

[12] J.-H. Kim, T.-Y. Seong, K.-B. Chung, C. S. Moon, J. H. Noh, H.-J. Seok, H.-K. Kim, *J. Power. Sources* **2019**, *418*, 152.

[13] J. Bing, S. Huang, A. W. Y. Ho-Baillie, *Energy Techno.* **2019**, 1901114.

[14] J.-W. Lee, N.-G. Park, *Adv. Energy Mater.* **2019**, *10*, 1903249.

[15] R. Wang, M. Mujahid, Y. Duan, Z.-K. Wang, J. Xue, Y. Yang, *Adv. Funct. Mater.* **2019**, *29*, 1808843.

[16] S. Liu, Y. Guan, Y. Sheng, Y. Hu, Y. Rong, A. Mei, H. Han, *Adv. Energy Mater.* **2019**, 1902492.

[17] C. H. Ng, H. N. Lim, S. Hayase, Z. Zainal, N. M. Huang, *Renewable Sustainable Energy Rev.* **2018**, *90*, 248.

[18] C. R. Kalaiselvi, N. Muthukumarasamy, D. Velauthapillai, M. Kang, T. S. Senthil, *Mater. Lett.* **2018**, *219*, 198.

[19] M. S. Jamal, M. S. Bashar, A. K. M. Hasan, Z. A. Almutairi, H. F. Alharbi, N. H. Alharthi, M. R. Karim, H. Misran, N. Amin, K. Bin Sopian, M. Akhtaruzzaman, *Renewable Sustainable Energy Rev.* **2018**, *98*, 469.

[20] J. H. Heo, H. J. Han, D. Kim, T. K. Ahn, S. H. Im, *Energy Environ. Sci.* **2015**, *8*, 1602.

[21] W. Ke, G. Fang, J. Wan, H. Tao, Q. Liu, L. Xiong, P. Qin, J. Wang, H. Lei, G. Yang, M. Qin, X. Zhao, Y. Yanfa, *Nat. Commun.* **2015**, *6*, 6700.

[22] Z. Zhu, Y. Bai, T. Zhang, Z. Liu, X. Long, Z. Wei, Z. Wang, L. Zhang, J. Wang, F. Yan, S. Yang, *Angew. Chem.* **2014**, *126*, 12779.

[23] A. Mei, X. Li, L. Liu, Z. Ku, T. Liu, Y. Rong, M. Xu, M. Hu, J. Chen, Y. Yang, M. Grätzel, H. Han, *Science* **2014**, *345*, 295.

[24] J. Yang, B. D. Siempelkamp, D. Liu, T. L. Kelly, *ACS Nano* **2015**, *9*, 1955.

[25] B. Hailegnaw, S. Kirmayer, E. Edri, G. Hodes, D. Cahen, *J. Phys. Chem. Lett.* **2015**, *6*, 1543.

[26] A. M. A. Leguy, Y. Hu, M. Campoy-Quiles, M. I. Alonso, O. J. Weber, P. Azarhoosh, M. V. Schilfgaarde, M. T. Weller, T. Bein, J. Nelson, P. Docampo, *Chem. Mater.* **2015**, *27*, 3397.

[27] R. K. Misra, S. Aharon, B. Li, D. Mogilyansky, I. Visoly-Fisher, L. Etgar, E. A. Katz, *J. Phys. Chem. Lett.* **2015**, *6*, 326.

[28] C. C. Stoumpos, C. D. Malliakas, M. G. Kanatzidis, *Inorg. Chem.* **2013**, *52*, 9019.

[29] E. T. Hoke, D. J. Slotcavage, E. R. Dohner, A. R. Bowring, H. I. Karunadasa, M. D. McGehee, *Chem. Sci.* **2015**, *6*, 613.

[30] Z. Xiao, Y. Yuan, Y. Shao, Q. Wang, Q. Dong, C. Bi, P. Sharma, A. Gruverman, J.

Huang, *Nat. Mater.* **2015**, *14*, 193.

[31] B. Conings, J. Drijkoningen, N. Gauquelin, A. Babayigit, J. D'Haen, L. D'Olieslaeger, A. Ethirajan, J. Verbeeck, J. Manca, E. Mosconi, *Adv. Energy Mater.* **2015**, *5*, 1500477.

[32] T. M. Koh, K. Fu, Y. Fang, S. Chen, T. C. Sum, N. Mathews, S. G. Mhaisalkar, P. P. Boix, T. Baikie, *J. Phys. Chem.* C **2014**, *118*, 16458.

[33] G. E. Eperon, S. D. Stranks, C. Menelaou, M. B. Johnston, L. M. Herz, H. J. Snaith, *Energy Environ. Sci.* **2014**, *7*, 982.

[34] S. Pang, H. Hu, J. Zhang, S. Lv, Y. Yu, F. Wei, T. Qin, H. Xu, Z. Liu, G. Cui, *Chem. Mater.* **2014**, *26*, 1485.

[35] N. Pellet, P. Gao, G. Gregori, T. Y. Yang, M. K. Nazeeruddin, J. Maier, M. Grätzel, *Angew. Chem.* **2014**, *126*, 3215.

[36] J.-W. Lee, D.-J. Seol, A.-N. Cho, N.-G. Park, *Adv. Mater.* **2014**, *26*, 4991.

[37] N. J. Jeon, J. H. Noh, W. S. Yang, Y. C. Kim, S. Ryu, J. Seo, S. I. Seok, *Nature* **2015**, *517*, 476.

[38] A. Binek, F. C. Hanusch, P. Docampo, T. Bein, *J. Phys. Chem. Lett.* **2015**, *6*, 1249.

[39] D. P. McMeekin, G. Sadoughi, W. Rehman, G. E. Eperon, M. Saliba, M. T. Hoerantner, A. Haghighirad, N. Sakai, L. Korte, B. Rech, M. B. Johnston, L. M. Herz, H. J. Snaith, *Science* **2016**, *351*, 151.

[40] J.-W. Lee, D.-H. Kim, H.-S. Kim, S.-W. Seo, S. M. Cho, N.-G. Park, *Adv. Energy Mater.* **2015**, *5*, 1501310.

[41] M. Saliba, T. Matsui, J.-Y. Seo, K. Domanski, J.-P. Correa-Baena, M. K. Nazeeruddin, S. M. Zakeeruddin, W. Tress, A. Abate, A. Hagfeldt, M. Grätzel, *Energy Environ. Sci.* **2016**, 9, 1989.

[42] Huang, C. Zhan, S.-H. Wang, J.-Z. Zhou, J.-W. Yan, B.-W. Mao, Z.-Q. Tian, J. Am. Chem. Soc. 2019, 141, 1665.

[43] W. Rehman, D. P. McMeekin, J. B. Patel, R. L. Milot, M. B. Johnston, H. J. Snaith, L. M. Herz, *Energy Environ. Sci.* **2017**, *10*, 361.

[44] Y. Zhou, M. Yang, O. S. Game, W. Wu, J. Kwun, M. A. Strauss, Y. Yan, J. Huang, K. Zhu, N. P. Padture, *ACS Appl. Mater. Interfaces* **2016**, *8*, 2232.

[45] J. Lu, X. Lin, X. Jiao, T. Gengenbach, A. D. Scully, L. C. Jiang, B. Tan, J. Sun, B. Li, N. Pai, U. Bach, A. N. Simonov, Y.-B. Cheng, *Energy Environ. Sci.* **2018**, *11*, 1880.

[46] C. Yi, J. Luo, S. Meloni, A. Boziki, N. Ashari-Astani, C. Grätzel, S. M. Zakeeruddin, U. Röthlisberger, M. Grätzel, *Energy Environ. Sci.* **2016**, *9*, 656.

[47] D.-Y. Son, J.-W. Lee, Y. J. Choi, I.-H. Jang, S. Lee, P. J. Yoo, H. Shin, N. Ahn, M. Choi, D. Kim, N.-G. Park, *Nat. Energy* **2016**, *1*, 16081.

[48] T. Leijtens, G. E. Eperon, S. Pathak, A. Abate, M. M. Lee, H. J. Snaith, *Nat. Commun.* **2013**, *4*, 2885.

[49] J. You, L. Meng, T. B. Song, T. F. Guo, Y. Yang, W. H. Chang, Z. Hong, H. Chen, H. Zhou, Q. Chen, Y. Liu, N. D. Marco, Y. Yang, *Nat. Nanotechnol.* **2016**, *11*, 75.

[50] V. M. Goldschmidt, *Naturwissenschaften* **1926**, *14*, 477.

[51] W. Travis, E. N. K. Glover, H. Bronstein, D. O. Scanlon, R. G. Palgrave, *Chem. Sci.* **2016**, *7*, 4548.

[52] C. Li, X. Lu, W. Ding, L. Feng, Y. Gao, Z. Guo, *Acta Cryst.* **2008**, *64*, 702.

[53] C. J. Bartel, C. Sutton, B. R. Goldsmith, R. Ouyang, C. B. Musgrave, L. M. Ghiringhelli, M. Scheffler, *Sci. Adv.* **2019**, *5*, eaav0693.

[54] Q. Sun, W.-J. Yin, *J. Am. Chem. Soc.* **2017**, *139*, 14905.

[55] L. Q. Jiang, J. K. Guo, H. B. Lin, M. Zhu, X. Zhou, P. Wu, C. H. Li, *J. Phys. Chem. Solids* **2006**, *67*, 1531.

[56] G. Kieslich, S. Sun, A. K. Cheetham, *Chem. Sci.* **2015**, 6, 3430

[57] Z. Liu, J. Chang, Z, Lin, L. Zhou, Z. Yang, D. Chen, C. Zhang, S. Liu, Y. Hao, *Adv. Energy Mater.* **2018**, *8*, 1703432.

[58] Y. Kato, L. K. Ono, M. V. Lee, S. Wang, S. R. Raga, Y. Qi, *Adv. Mater. Interfaces,* **2015**, *2*, 1500195.

[59] K. Domanski, J.-P. Correa-Baena, N. Mine, M. K. Nazeeruddin, A. Abate, M. Saliba, W. Tress, A. Hagfeldt, M. Grätzel, *ACS Nano,* **2016**, *10*, 6306.

[60] R. Cheacharoen, C. C. Boyd, G. F. Burkhard, T. Leijtens, J. A. Raiford, K. A. Bush, S. F. Bent, M. D. McGehee, *Sustainable Energy Fuels* **2018**, *2*, 2398.

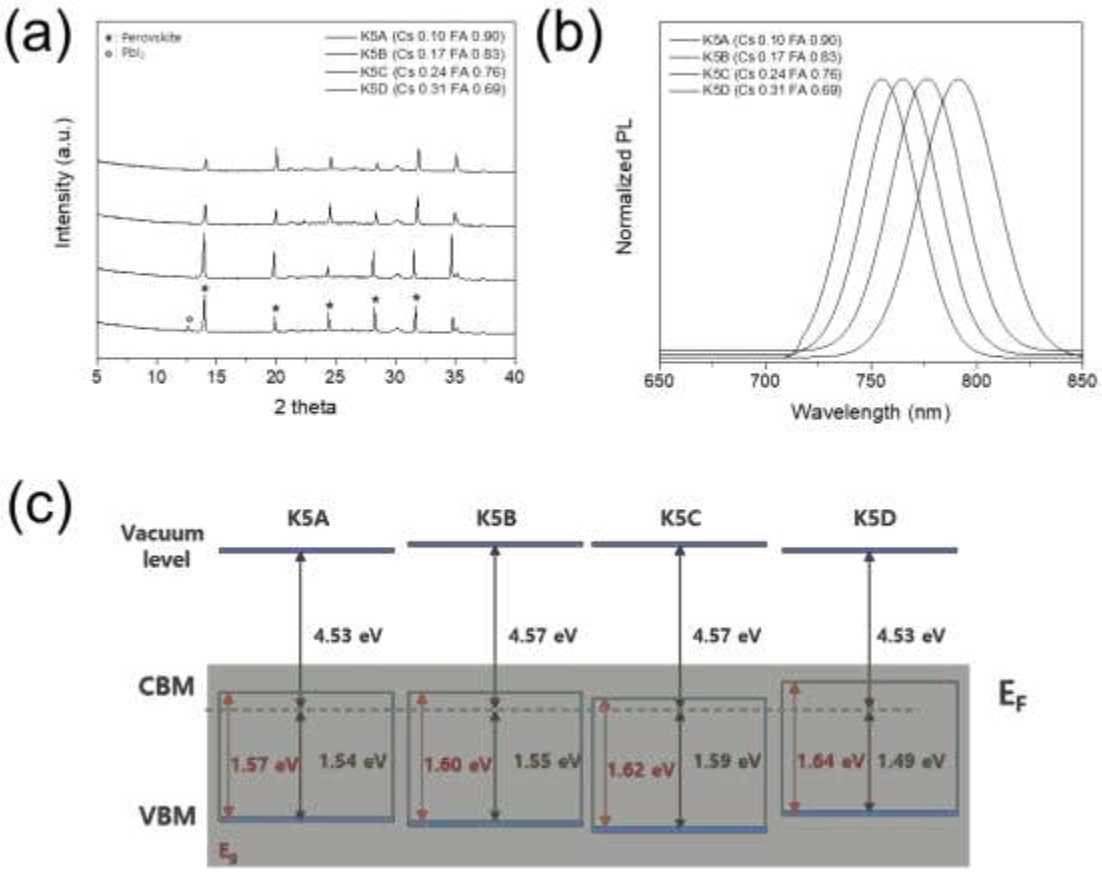

Figure 1. (a) X-ray diffraction (XRD) patterns, and (b) photoluminescence (PL) spectra, of the $Cs_xFA_{1-x}Pb(I_{0.94}Br_{0.06})_3$ films. (c) Energy band diagram of the perovskite films with different Cs and FA molar ratios.

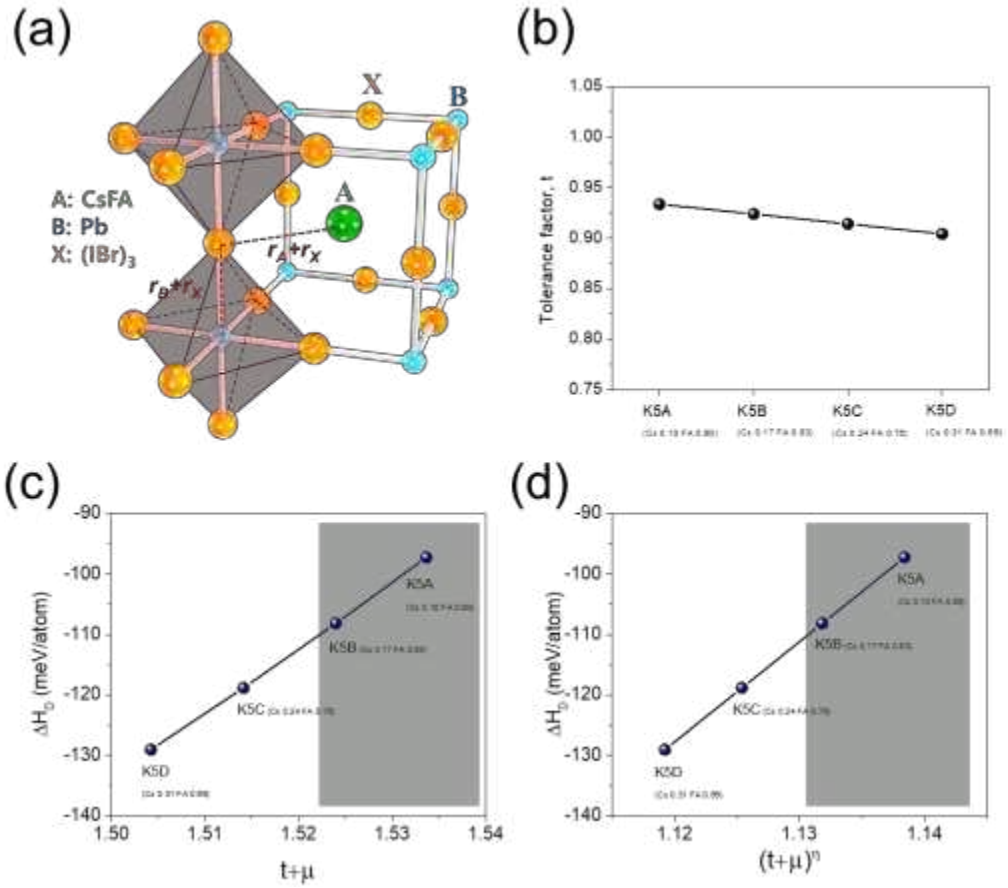

Figure 2. (a) The local atomic structure of cubic perovskite. (b) Tolerance factors of the K5 series perovskite. Decomposition energies of perovskite compounds dependent on (c) t+μ, and (d) $(t+\mu)^{\eta}$.

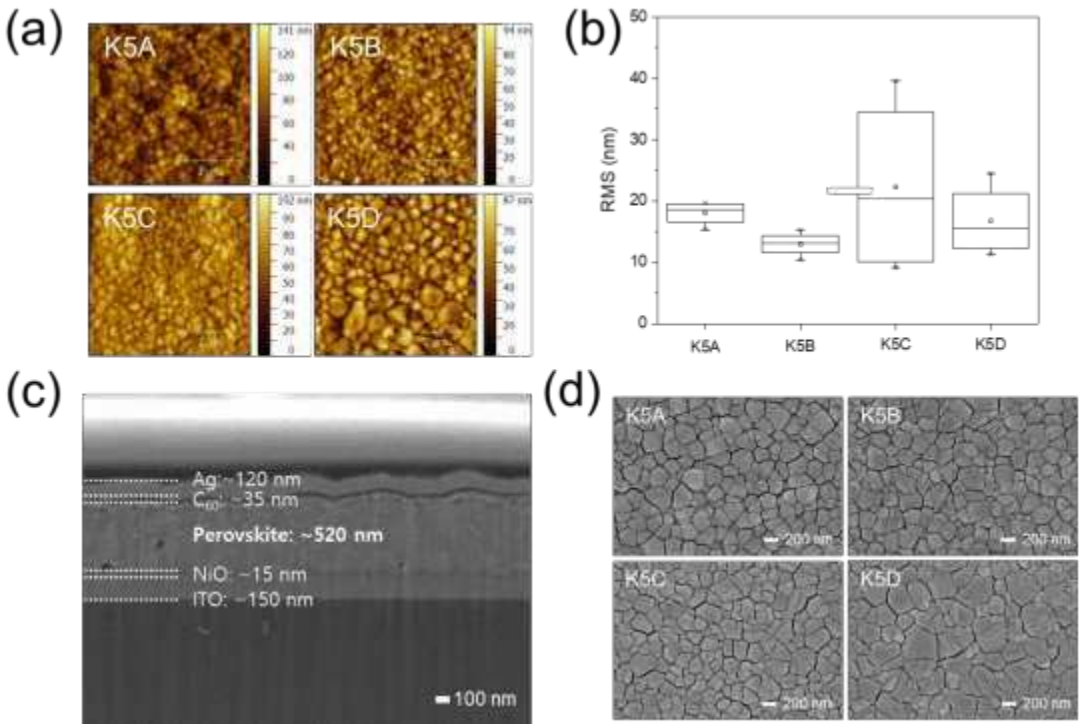

Figure 3. (a) AFM images, and (b) root mean square roughness (RMS) values of perovskite films. (c) Cross-sectional SEM images of planar-structured PSC employing a K5B ($Cs_{0.17}FA_{0.83}Pb(I_{0.94}Br_{0.06})_3$) active layer. (d) Surface SEM images of K5 series perovskite films.

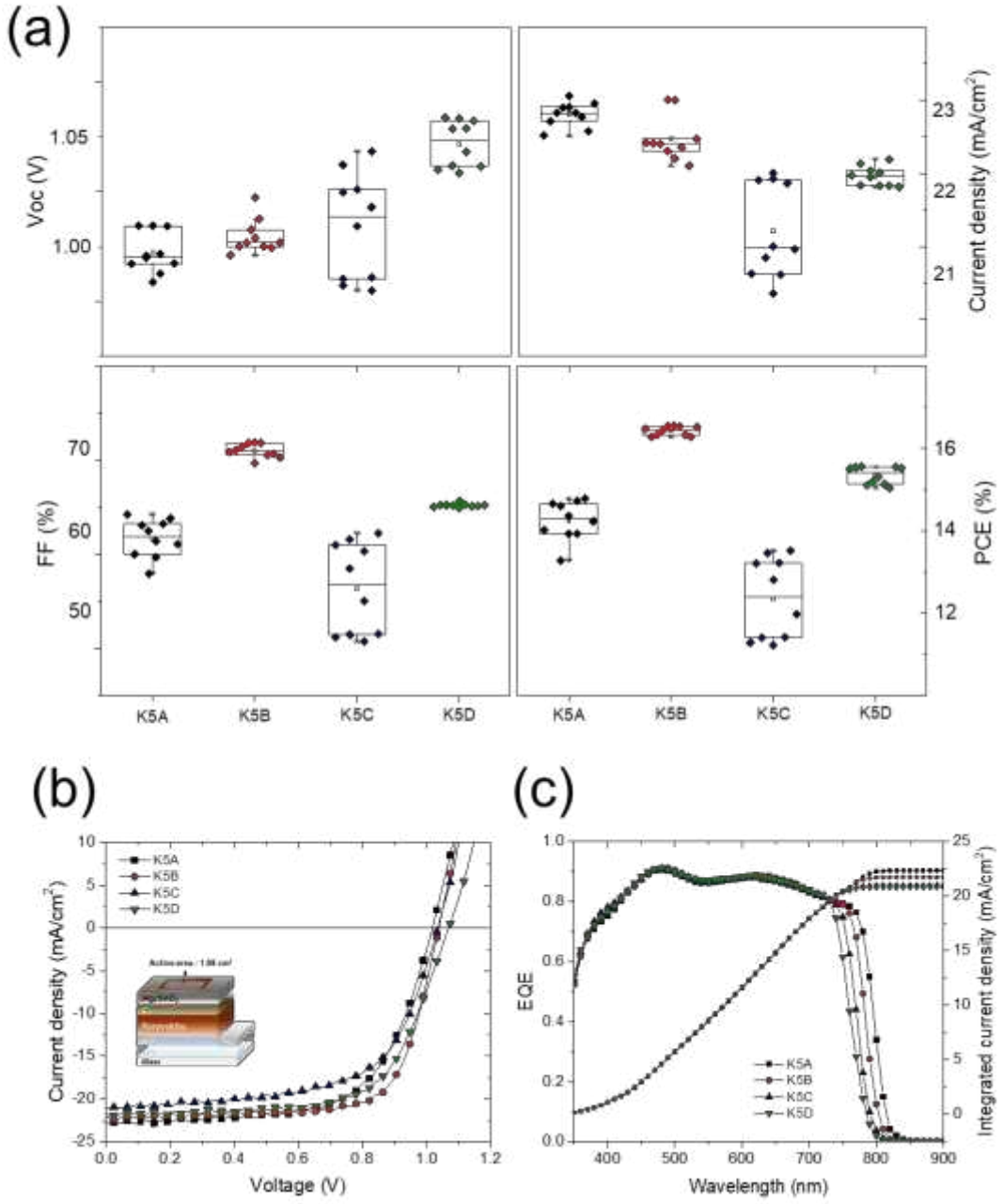

Figure 4. (a) Photovoltaic performance statistics of PSCs using K5 series perovskite with an active area of 1.08 cm^2. (b) J–V curves, and (c) EQE spectra of PSCs using the K5 series perovskite active layers.

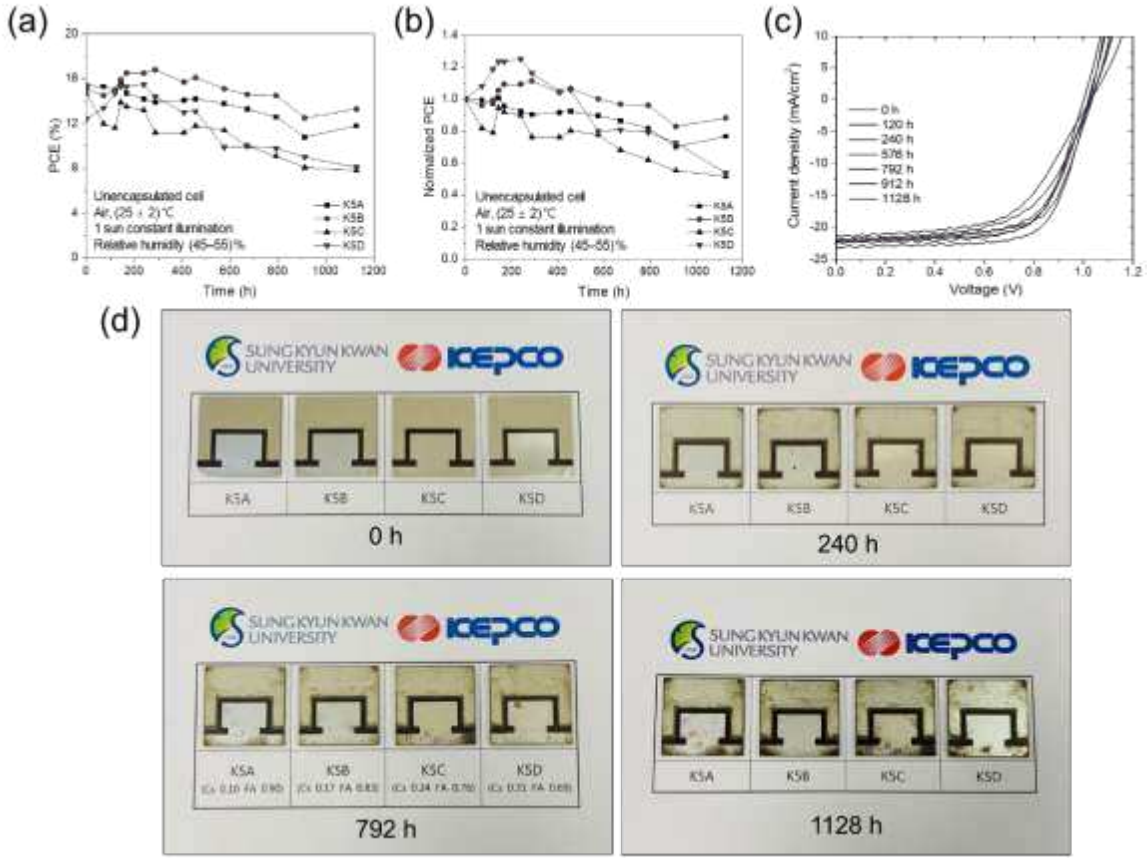

Figure 5. Long-term stability of $Cs_xFA_{1-x}Pb(I_{0.94}Br_{0.06})_3$ solar cells: (a) PCE, and (b) normalized PCE of $Cs_xFA_{1-x}Pb(I_{0.94}Br_{0.06})_3$ solar cells as a function of time under < 55% RH. (c) J–V curves of K5B ($Cs_{0.17}FA_{0.83}Pb(I_{0.94}Br_{0.06})_3$) solar cell during 1,128 h. (d) Photographs of PSCs with K5 series perovskite active layer with different storage time.

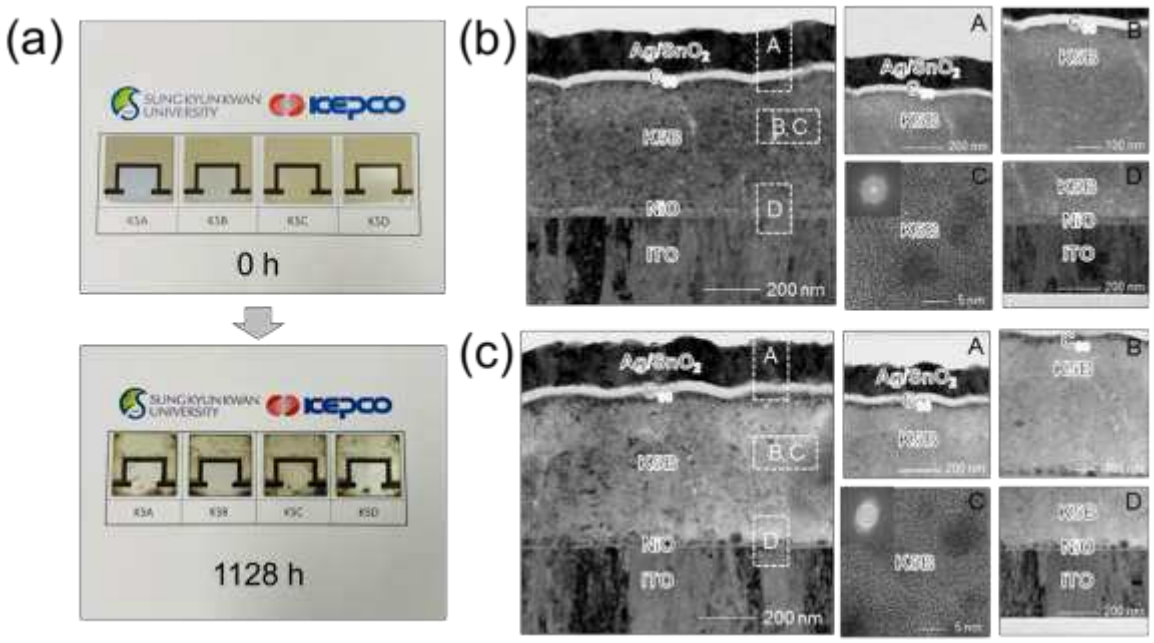

Figure 6. (a) Photographs of PSCs with K5 series perovskite active layer after initial fabrication and stability test during 1,128 h. Cross-sectional TEM image of (b) fresh PSC, and (c) PSC after 1,128 h using K5B ($Cs_{0.17}FA_{0.83}Pb(I_{0.94}Br_{0.06})_3$) perovskite active layers. Enlarged TEM images were obtained of A ($Ag/SnO_2/C_{60}$/K5B perovskite), B (C_{60}/K5B perovskite), C (K5B perovskite with an insert of FFT patterns), and D (K5B perovskite/NiO/ITO), respectively.

Table captions

Table 1. Summary of Cs/FA ratios and band energies of the K5 series perovskite compounds.

Sample	Cs/FA ratio	Optical bandgap (eV)	VBM (eV)	CBM (eV)	Fermi level (eV)
K5A	0.11	1.57	-6.07	-4.50	-4.53
K5B	0.20	1.60	-6.12	-4.52	-4.57
K5C	0.32	1.62	-6.16	-4.54	-4.57
K5D	0.45	1.64	-6.02	-4.38	-4.53

Table 2. Calculated structural factors and decomposition energies of the K5 series perovskite compounds.

Sample	Tolerance factor, t	Octahedral factor, μ	Atomic packing fraction, η	t+μ	$(t+\mu)^{\eta}$	Decomposition Energy (meV/atom)
K5A	0.934	0.600	0.303	1.534	1.138	-97.3
K5B	0.924	0.600	0.294	1.524	1.132	-108.2
K5C	0.914	0.600	0.285	1.514	1.125	-118.9
K5D	0.904	0.600	0.276	1.504	1.119	-129.1

Table 3. Photovoltaic parameters derived from current–voltage (J–V) measurements of the PSCs using K5 series perovskite active layers.

Sample	Voc (V)	Jsc (mA/cm^2)	FF (%)	PCE (%)
K5A	1.01	22.7	63.8	14.8
K5B	1.03	22.2	71.8	16.5
K5C	1.03	21.0	62.2	13.5
K5D	1.08	22.0	65.2	15.5

Table 4. Photovoltaic parameters of the PSCs using K5B ($Cs_{0.17}FA_{0.83}Pb(I_{0.94}Br_{0.06})_3$) perovskite active layers as a function of time.

Time (h)	Voc (V)	Jsc (mA/cm^2)	FF (%)	PCE (%)
0	1.00	22.1	68.5	15.1
120	1.01	22.3	66.3	15.0
240	1.02	23.0	70.3	16.5
576	1.03	21.8	67.3	15.1
792	1.02	22.2	63.4	14.5
912	1.02	21.3	57.2	12.5
1128	1.03	21.9	58.8	13.3
Rel. degradation (%)	-3.0	0.9	14.2	11.9

The effect of Cs/FA ratio on the long-term stability of mixed cation perovskite solar cells

*Dong-Hyeok Choi, Hae-Jun Seok, Do-Hyung Kim, Su-Kyung Kim, Bo Hou, and Han-Ki Kim**

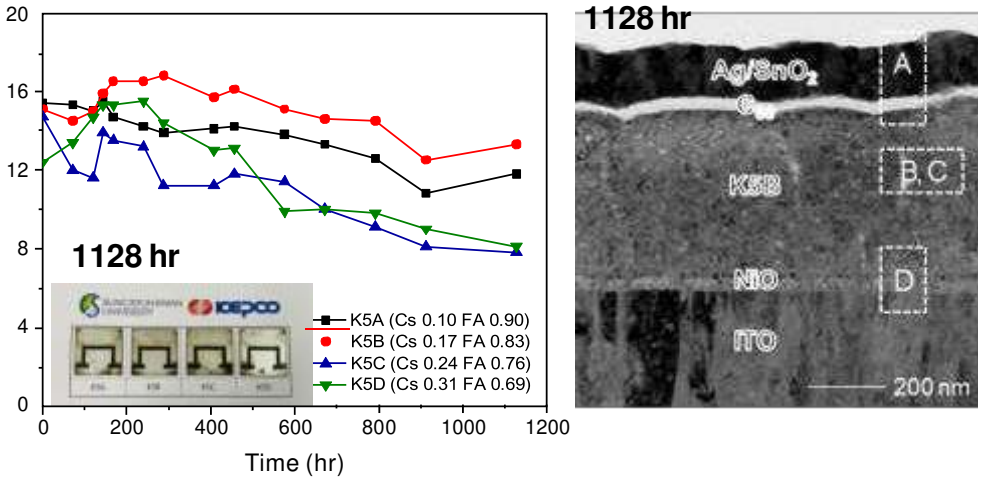

Power conversion efficiency of the $Cs_xFA_{1-x}Pb(I_{0.94}Br_{0.06})_3$-based perovskite solar cells as a function of time and a cross-sectional TEM image to demonstrate stable interface of K5B active layer-based perovskite solar cell after 1128 hr.